

Understanding high domain wall velocities in spin valves with perpendicular current injection and further boosting by transverse magnetic fields

Mei Li,¹ Zhong An,² and Jie Lu^{2,*}

¹Physics Department, Shijiazhuang University, Shijiazhuang, Hebei 050035, China
²College of Physics and Information Engineering, Hebei Advanced Thin Films Laboratory,
 Hebei Normal University, Shijiazhuang 050024, China
 (Dated: January 29, 2019)

In this work, transverse domain wall (TDW) dynamics in long and narrow spin valves with perpendicular current injections is investigated based on Lagrangian formalism as well as appropriate dissipation terms. First the spin-transfer torque (STT) coefficients are assumed to be independent of $\mathbf{m} \cdot \mathbf{m}_p$ (\mathbf{m} and \mathbf{m}_p are normalized magnetization vectors in free and pinned layers of spin valves, respectively). Three typical choices of polarizer (\mathbf{m}_p) are considered: parallel, perpendicular and planar-transverse. For each case, the dynamical behavior of Walker-profile TDWs is studied and the corresponding stability analysis is performed. The results for parallel and perpendicular polarizers perfectly explain the existing simulation findings. For planar-transverse polarizers, stable traveling-wave motion of TDWs with finite velocity can only survive for strong enough spin polarization of charge current with $\mathbf{m} \cdot \mathbf{m}_p$ -dependent STT coefficients (for example, Slonczewski's original description). It turns out that the planar-transverse polarizer has nearly the same current efficiency as the perpendicular polarizer. More importantly, in this case the wall has infinite "differential mobility" around the onset of stable wall excitation. Further boosting of TDWs by external uniform transverse magnetic fields is also investigated with help of one dimensional asymptotic expansion method.

I. INTRODUCTION

In the past decades, tremendous progress in fabrication technology of non-volatile magnetic nanodevices has led to a great revolution in modern information industry[1–3]. In these nanodevices, magnetic domains with different orientations are candidates of zeros and ones in binary world. The intermediate region separating these domains are the domain walls (DWs) which are the main focus in the field of nanomagnetism since their motion leads to the transformation between 0 and 1[4–8]. DWs can be driven to move by magnetic fields (damping mechanism)[9], spin-polarized currents (spin-transfer process)[10–13] or temperature gradient (entropy increase)[14, 15], etc. Among them, current-induced DW motion should be the easiest to implement and manipulate in real experiment and engineering.

Historically, spin-transfer torque (STT) was first calculated in a magnetic multilayer in which the two ferromagnetic (FM) layers are single-domained with current perpendicular to the plane (CPP) configuration[11]. After taking WKB approximation and ballistic assumption, as well as averaging the spin fluxes over the spacer, the STT therein is proportional to $\mathbf{m} \times (\mathbf{m} \times \mathbf{m}_p)$ in which \mathbf{m} and \mathbf{m}_p are normalized magnetization vectors in the thin (free) and thick (pinned) layers. This term is the so-called Slonczewski torque (SLT). In fact, another torque term ($\propto \mathbf{m} \times \mathbf{m}_p$) must exist due to the inevitably imperfections of the above processing procedure and is usually called the field-like torque (FLT) since now \mathbf{m}_p acts like an effective field. Later in magnetic nanostrips with currents flowing in strip plane (CIP), adiabatic and nonadiabatic STTs are proposed (both proportional to spacial gradient of magnetization) which can be viewed as the continuous limits of SLT and FLT, respectively[12, 13]. It turns out that the adiabatic STT induces the initial DW movement but the final wall ve-

locity is determined by the nonadiabatic STT. However, since the exchange interaction avoids abrupt variation of magnetization, CIP current density of several 10^8 A/cm² only leads to DW velocity around 100 m/s.

To further increase the current efficiency, long and narrow spin valves (LNSVs) or magnetic tunneling junctions (MTJs) with CPP configuration are proposed to be the host systems[16–18]. In these multilayers, a DW in the free layer is driven to move along the long axis by the spin-polarized current filtered by the pinned layer (polarizer). Depending on the magnetization orientation in the pinned layer, the LNSVs or MTJs are classified as parallel, perpendicular and planar-transverse polarizer cases. Early numerical simulations focus on the former two cases and only SLTs are considered[19, 20]. It turned out that the current efficiency can not be increased too much. In 2009, a significant breakthrough[21] was made by Khvalkovskiy *et. al.* in which numerical simulations with both SLT and FLT (and $\mathbf{m} \cdot \mathbf{m}_p$ -independent STT coefficients) reveal that for parallel polarizers, to achieve a DW velocity of 10^2 m/s, the CPP current density is lowered to 10^7 A/cm². While for perpendicular polarizers, the CPP current density is further decreased to 10^6 A/cm² to achieve the same wall velocity.

Inspired by this numerical finding, two series of experimental verification works were carried out. First, in LNSVs[22] and half-ring MTJs[23–25] with perpendicular polarizers and CPP configuration, transport measurements confirms that DW can propagate with velocities as high as 500-800 m/s at current density below 10^7 A/cm². Second, in ZigZag LNSVs with CIP configuration high DW velocities (150-600 m/s) are obtained for current densities of $2 \times 10^7 \sim 5 \times 10^7$ A/cm² by using photoemission electron microscopy (PEEM) combined with X-ray magnetic circular dichroism (XMCD)[26–29]. Vertical spin current coming with the spin flux transfor-

mation from the pinned layer to the free layer via the spacer is suggested to provide a potential explanation for this velocity increase at low current densities. In both half-ring MTJs with CPP configuration and ZigZag LNSVs with CIP configuration, the Oersted field may have strong effect on magnetization dynamics in free layer[23, 24, 27–29].

To understand these numerical and experimental results, in 2013 a systematic theoretical study based on Lagrangian formalism was proposed[30]. However the analytics is not exactly corresponding to existing simulations since in the theoretical work STT coefficients are proportional to the spin polarization factor $g \equiv [-4 + (1 + P)^3(3 + \mathbf{m} \cdot \mathbf{m}_p)/(4P^{3/2})]^{-1}$ (see Slonczewski's original description in Ref.[11]) rather than merely the spin polarization of current (P) in Khvalkovskiy's work[21]. In this paper, first we construct appropriate Lagrangian that well describes the case in Khvalkovskiy's work (with $\mathbf{m} \cdot \mathbf{m}_p$ -independent STT coefficients). The resulting Euler-Lagrange equation is the well-known Landau-Lifshitz-Gilbert (LLG) equation. Based on Walker profiles and within one-dimensional collective coordinate model (1D-CCM)[31], DW dynamics in LNSVs for all three typical polarizers are investigated. Analytics for parallel and perpendicular polarizers provide reasonable explanations to existing numerical data. While the results for planar-transverse polarizers with $\mathbf{m} \cdot \mathbf{m}_p$ -dependent STT coefficients present another way to efficiently induce DW motion in LNSVs with CPP currents. Also, DWs in free layers of LNSVs can be further boosted by uniform transverse magnetic fields (UTMFs). With the help of 1D asymptotic expansion method (1D-AEM)[32–36], the boosting effects of UTMFs on DWs are studied, which constitutes the second part of this work.

The paper is organized as follows. In Sec. II, the Lagrangian with $\mathbf{m} \cdot \mathbf{m}_p$ -independent STT coefficients and dissipation terms are introduced. A set of dynamical equations for a polarizer with general orientation are obtained and serve as the startpoint of our work. In Sec. III and IV, DW dynamics under parallel and perpendicular polarizers are investigated and compared with existing simulations. In addition, DW dynamics under planar-transverse polarizers are investigated in Sec. V for STT coefficients both independent and dependent on $\mathbf{m} \cdot \mathbf{m}_p$. Furthermore, the boosting effects of UTMFs on DW motion in LNSVs are studied in Sec. VI. Finally the concluding remarks are provided in Sec. VII.

II. LAGRANGIAN FORMALISM AND DYNAMICAL EQUATIONS

We consider a LNSV with CPP configuration, as shown in Fig. 1. It is composed of three layers: a free FM layer with tunable magnetization texture, a nonmagnetic (NM) metallic spacer and a pinned FM layer with a fixed magnetization orientation. The global Cartesian coordinate system in real space is as follows: \mathbf{e}_z is along the long axis of this LNSV, \mathbf{e}_y follows the electron flow direction (from pinned to free layer)

and $\mathbf{e}_x = \mathbf{e}_y \times \mathbf{e}_z$. The pinned layer is usually made of hard magnetic materials and the orientation of its fixed magnetization (\mathbf{m}_p) has three typical choices: (a) $\mathbf{m}_p = \mathbf{m}_z$ (parallel polarizer), (b) $\mathbf{m}_p = \mathbf{m}_y$ (perpendicular polarizer) and (c) $\mathbf{m}_p = \mathbf{m}_x$ (planar-transverse polarizer). The electron flows from the pinned FM layer to the free FM layer via the metallic spacer with density $J_e (> 0)$, which makes the charge current $J_{\text{charge}} = -J_e \mathbf{m}_y$.

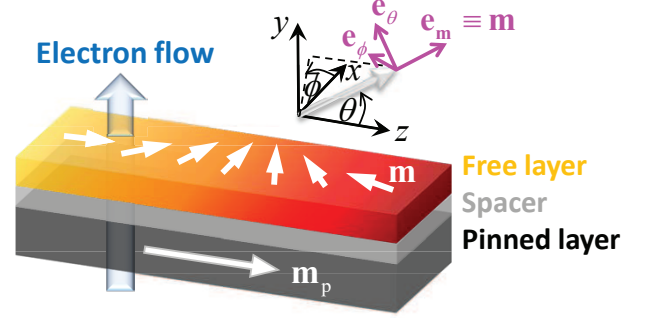


FIG. 1. (Color online) Sketch of a LNSV with CPP configuration under consideration. It is composed of three layer structures: a pinned FM layer, a NM metallic spacer and a free FM layer. The pinned layer has a fixed magnetization orientation with \mathbf{m}_p being the corresponding unit vector. A DW is nucleated in the free layer and can be driven to move along the long axis of the LNSV. $(\mathbf{e}_x, \mathbf{e}_y, \mathbf{e}_z)$ is the global Cartesian coordinate system in real space: \mathbf{e}_z is along the LNSV long axis, \mathbf{e}_y is along the electron flow direction (from pinned to free layer) and $\mathbf{e}_x = \mathbf{e}_y \times \mathbf{e}_z$. $(\mathbf{e}_m, \mathbf{e}_\theta, \mathbf{e}_\phi)$ forms the local spherical coordinate system associated with the magnetization vector in the free layer.

In the global Cartesian coordinate system, the unit vector of magnetization in free layer can be fully described by its polar angle θ and azimuthal angle ϕ . The associated local spherical coordinate system is denoted as $(\mathbf{e}_m, \mathbf{e}_\theta, \mathbf{e}_\phi)$, as shown in the right-up corner of Fig. 1. While the corresponding angles of the unit vector in the pinned layer are θ_p and ϕ_p , respectively. Considering the transition between $(\mathbf{e}_x, \mathbf{e}_y, \mathbf{e}_z)$ and $(\mathbf{e}_m, \mathbf{e}_\theta, \mathbf{e}_\phi)$, \mathbf{m}_p can be rewritten as

$$\mathbf{m}_p = p_m \mathbf{e}_m + p_\theta \mathbf{e}_\theta + p_\phi \mathbf{e}_\phi, \quad (1)$$

with

$$\begin{aligned} p_m &= \sin \theta_p \cos(\phi - \phi_p) \sin \theta + \cos \theta_p \cos \theta, \\ p_\theta &= \sin \theta_p \cos(\phi - \phi_p) \cos \theta - \cos \theta_p \sin \theta, \\ p_\phi &= -\sin \theta_p \sin(\phi - \phi_p). \end{aligned} \quad (2)$$

In the presence of CPP currents, the magnetic energy of the free layer includes the exchange, crystalline anisotropy, magnetostatic and FLT-induced effective potential energies. In thin enough strips, most of the nonlocal magnetostatic energy can be described by local quadratic terms of $M_{x,y,z}$ by means of three average demagnetization factors[34]. Thus in 1D approximation, one has

$$\mathcal{E}[\mathbf{m}] = \mathcal{E}_0[\mathbf{m}] - \mu_0 M_s b_J p_m, \quad (3)$$

with

$$\mathcal{E}_0[\mathbf{m}] = J \left(\frac{\partial \mathbf{m}}{\partial z} \right)^2 + \mu_0 M_s^2 \left(-\frac{1}{2} k_E m_z^2 + \frac{1}{2} k_H m_y^2 \right), \quad (4)$$

in which J is the exchange stiffness, μ_0 is the permeability of vacuum, $k_E(k_H)$ is the total anisotropy coefficient along the easy (hard) axis of the free layer and M_s is its saturation magnetization. In addition, $b_J = \xi_{\text{CPP}} a_J$ where ξ_{CPP} describes the relative strength of FLT over SLT. Here we choose the “ $\mathbf{m} \cdot \mathbf{m}_p$ -independent” form of a_J in the simulation work in Ref.[21], that is, $a_J = \hbar J_e P / (g_e d e M_s)$, where d is the thickness of free layer, $e (> 0)$ is the absolute charge of electron, g_e is the electron g-factor and P is the spin polarization of the current. This should be a reasonable assumption based on transport calculations in recent years[37, 38].

The CPP-current-driven dynamics of TDW in the free layer can be described by the Lagrangian $L = \int \mathcal{L} d^3 \mathbf{r}$ with \mathcal{L} being the Lagrangian density of this magnetic system

$$\mathcal{L} = \frac{\mu_0 M_s}{\gamma} \dot{\phi} \cdot (1 - \cos \theta) - \mathcal{E}, \quad (5)$$

in which $\gamma = e g_e / (2 m_e)$ is the electron gyromagnetic ratio and a dot means $\partial / \partial t$. To describe the Gilbert damping and the SLT-induced anti-damping processes, an extra dissipation functional $F = \int \mathcal{F} d^3 \mathbf{r}$ is then introduced as

$$\mathcal{F} = \frac{\alpha}{2} \frac{\mu_0 M_s}{\gamma} (\dot{\theta}^2 + \dot{\phi}^2 \sin^2 \theta) - \mu_0 M_s a_J (p_\theta \sin \theta \dot{\phi} - p_\phi \dot{\theta}). \quad (6)$$

The resulting generalized Euler-Lagrangian equation

$$\frac{d}{dt} \left(\frac{\delta \mathcal{L}}{\delta \dot{X}} \right) - \frac{\delta \mathcal{L}}{\delta X} + \frac{\delta \mathcal{F}}{\delta \dot{X}} = 0, \quad X = \theta, \phi \quad (7)$$

provides the well-known LLG equation

$$\begin{aligned} \frac{\partial \mathbf{m}}{\partial t} = & -\gamma \mathbf{m} \times \mathbf{H}_{\text{eff}} + \alpha \mathbf{m} \times \frac{\partial \mathbf{m}}{\partial t} \\ & - \gamma a_J \mathbf{m} \times (\mathbf{m} \times \mathbf{m}_p) - \gamma b_J \mathbf{m} \times \mathbf{m}_p, \end{aligned} \quad (8)$$

with $\mathbf{H}_{\text{eff}} = -(\mu_0 M_s)^{-1} \delta \mathcal{E}_0 / \delta \mathbf{m}$. The four terms in the right-hand side of above equation are the gyro precession, Gilbert damping, Slonczewski and field-like torques, respectively.

Early simulations confirmed that in FM nanostrips with small enough cross section area, TDWs have the lowest energy among all meta-stable states[39, 40]. In 2012, further simulations revealed that the stability range of TDW in the free layer of a LNSV can be shifted towards larger cross section area compared to single strip, due to a magnetostatic screening effect between the free and pinned layers[41]. It can be easily checked that in static case ($J_e = 0$), the Walker profile

$$\text{In tan} \frac{\theta(z)}{2} = \frac{z - z_0}{\Delta_0}, \quad \phi = n\pi, \quad \Delta_0 = \frac{l_0}{\sqrt{k_E}} \quad (9)$$

in easy plane (xz -plane) is the direct consequence of Eq. (7) with $X \equiv \theta$ and $\dot{\phi} \equiv 0$, in which $l_0 \equiv \sqrt{2J / (\mu_0 M_s^2)}$ is the

exchange length of the free layer. Therefore the configuration space of TDWs in this work is restricted to the generalized Walker profile

$$\text{In tan} \frac{\vartheta(z,t)}{2} = \eta \frac{z - q(t)}{\Delta(t)}, \quad \phi(z,t) \equiv \varphi(t), \quad (10)$$

in which the wall center position $q(t)$, tilting attitude $\varphi(t)$ and the wall width $\Delta(t)$ are the three collective coordinates in 1D-CCM. At last, $\eta = +1$ or -1 represents head-to-head (HH) or tail-to-tail (TT) TDWs, respectively.

In Eq. (7), by letting X take $q(t)$, $\varphi(t)$, $\Delta(t)$ successively, and integrating over the whole 1D space (i.e. $\int_{-\infty}^{+\infty} dz$), we obtain the following dynamic equations

$$\alpha \eta \frac{\dot{q}}{\Delta} + \dot{\phi} = \gamma \left(\frac{\pi}{2} a_J p_\phi + b_J \cos \theta_p \right), \quad (11)$$

$$\eta \frac{\dot{q}}{\Delta} - \alpha \dot{\phi} = \gamma M_s k_H \sin \varphi \cos \varphi + \gamma \left(a_J \cos \theta_p - \frac{\pi}{2} b_J p_\phi \right), \quad (12)$$

$$\frac{\pi^2 \alpha}{6} \frac{\dot{\Delta}}{\Delta} = \gamma M_s \left(\frac{l_0^2}{\Delta^2} - k_E - k_H \sin^2 \varphi \right) + \gamma \pi b_J \sin \theta_p \cos(\varphi - \phi_p). \quad (13)$$

This set of equations is the starting point for our investigations in this work. In all necessary calculations, the following magnetic parameters for Co are adopted for comparison with simulation works in Ref. [21]: $M_s = 1400$ kA/m, $J = 30 \times 10^{-12}$ J/m and $\alpha = 0.007$. Thus the exchange length $l_0 = 4.94$ nm. The geometry of free layer is $50 \times 3 \times 8000$ nm³, resulting in the three average demagnetization factors: $D_y = 0.917251$, $D_x = 0.082269$ and $D_z = 0.000480$. The crystalline anisotropy and edge roughness are both neglected, thus one has $k_E = D_x - D_z = 0.081789$ and $k_H = D_y - D_x = 0.834982$. Then $\Delta_0 = l_0 / \sqrt{k_E} = 17.3$ nm. For all three polarizer cases, the spin polarization is set as $P = 0.32$ and $\xi_{\text{CPP}} = 0.1$. Then the conversion coefficient from current density to SLT strength is $\kappa = a_J / J_e = \hbar P / (2 d e M_s) = 2.51 \times 10^{-6}$ Oe/(A/cm²).

III. DW DYNAMICS UNDER PARALLEL POLARIZER

In this case, $\mathbf{m}_p = \mathbf{m}_z$, thus $\theta_p = 0$ and then $p_\phi = 0$. The dynamical equations turn to

$$\frac{1 + \alpha^2}{\gamma} \frac{\eta \dot{q}}{\Delta} = \frac{k_H M_s}{2} \sin 2\varphi + (a_J + \alpha b_J), \quad (14)$$

$$\frac{1 + \alpha^2}{\gamma} \dot{\phi} = -\frac{\alpha k_H M_s}{2} \sin 2\varphi + (b_J - \alpha a_J), \quad (15)$$

$$\frac{\pi^2 \alpha}{6 \gamma M_s} \frac{\dot{\Delta}}{\Delta} = \frac{l_0^2}{\Delta^2} - k_E - k_H \sin^2 \varphi. \quad (16)$$

The first two equations reproduce Eq. (4) in Khvalkovskiy's work (see Ref. [21]) and the third one provides the TDW width. At $t = 0$, the TDW lies in the easy plane thus $\varphi|_{t=0} = m\pi$ ($m \in \mathbb{Z}$). The initial wall velocity is $v|_{t=0} = \eta\Delta_0\gamma a_J(1 + \alpha\xi_{\text{CPP}})/(1 + \alpha^2)$, which is mainly determined by SLT since $\alpha \ll 1$.

Next we focus on traveling-wave mode of TDW, thus $\dot{\varphi} = 0$ and $\dot{\Delta} = 0$. This leads to a FLT-determined steady wall velocity

$$\begin{aligned} v_0 &= \frac{\eta\Delta_1(\varphi_0)\gamma\xi_{\text{CPP}}a_J}{\alpha}, \\ \sin 2\varphi_0 &= \frac{2(\xi_{\text{CPP}} - \alpha)a_J}{\alpha M_s k_H}, \\ \Delta_1(\varphi_0) &= l_0(k_E + k_H \sin^2 \varphi_0)^{-1/2}. \end{aligned} \quad (17)$$

Obviously HH and TT TDWs acquire opposite velocities under the same electron flow.

Then we perform stability analysis to this traveling-wave solution. Suppose

$$\varphi = \varphi_0 + \delta\varphi, \quad |\delta\varphi| \ll |\varphi_0|, \quad (18)$$

$$\Delta = \Delta_1(\varphi_0) + \delta\Delta, \quad |\delta\Delta| \ll \Delta_1(\varphi_0). \quad (19)$$

Putting Eq. (18) into Eq. (15) and preserving only the first-order terms, one has

$$\frac{\partial(\delta\varphi)}{\partial t} = -\frac{\alpha\gamma M_s k_H \cos 2\varphi_0}{2(1 + \alpha^2)} \cdot \delta\varphi. \quad (20)$$

Obviously only when $\cos 2\varphi_0 > 0$, i.e. $|\varphi_0 - n\pi| < \pi/4$, the φ_0 -solution is stable. On the other hand, substituting Eq. (19) into Eq. (16) and after similar calculation, we have

$$\frac{\pi^2\alpha}{6\gamma M_s} \frac{\partial(\delta\Delta)}{\partial t} = -\frac{2l_0^2}{\Delta_1^2(\varphi_0)} \cdot \delta\Delta - \Delta_1(\varphi_0)k_H \sin 2\varphi_0 \cdot \delta\varphi. \quad (21)$$

Clearly, the $\Delta_1(\varphi_0)$ -solution should be stable when φ_0 is stable.

By requiring $|\sin 2\varphi_0| \leq 1$, the corresponding Walker threshold (under which traveling-wave mode survives) is $J_W = \alpha M_s k_H / (2\kappa|\xi_{\text{CPP}} - \alpha|) = 2.20 \times 10^8$ A/cm². Note that this is just the theoretical prediction based on the generalized Walker profile. Real simulations (see Fig. 1(b) of Ref. [21]) reveal that TDWs will disappear due to global-spin-transfer-induced domain excitation when $J_e > 2.4 \times 10^7$ A/cm² which is an order of magnitude smaller J_W . Thus in traveling-wave mode, at most one has $\sin^2 \varphi_0 \sim 10^{-2}$ and $\Delta_1(\varphi_0) \sim \Delta_0 = 17.3$ nm which keeps the TDW mobility (velocity versus current density) a constant value $\sim 1.09 \times 10^{-6}$ (m/s)/(A/cm²). This perfectly explains the linear dependence of wall velocity on current density in existing simulations. In Fig. 2, the analytical results in Eq. (17) for the magnetic parameters listed in the end of Sec. II are plotted by solid curves. Meantime, numerical data from Fig. 1(b) in Ref. [21] with the same geometric and magnetic parameters are indicated in Fig. 2(c) by solid squares. Obviously when TDWs exist ($J_e < 2.4 \times 10^7$ A/cm²), our theoretical results are in good agreement with the numerical simulations.

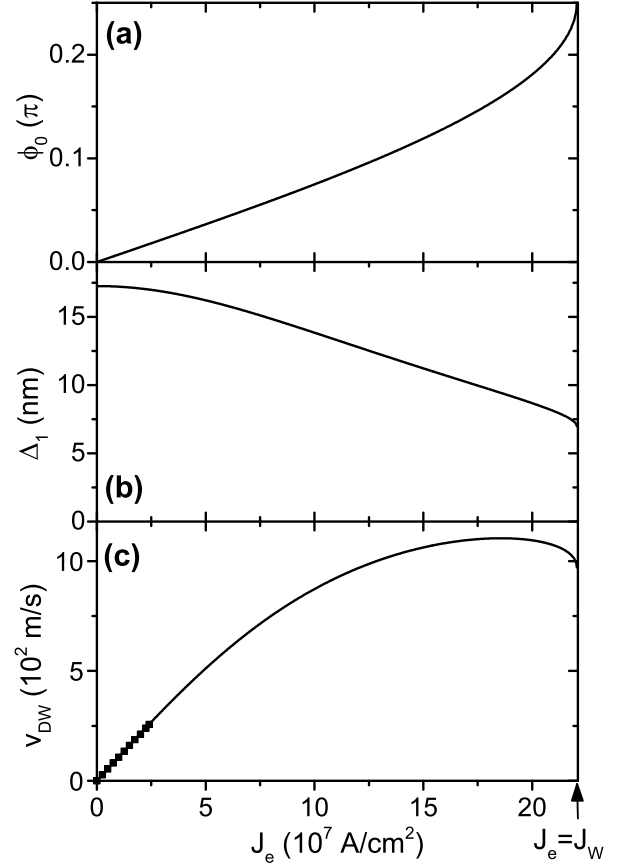


FIG. 2. Dependence of the tilting attitude (a), width (b) and velocity (c) of a DW on current density in a LNSV with CPP configuration and parallel polarizer ($\mathbf{m}_p = \mathbf{e}_z$). The free FM layer has a geometry of $50 \times 3 \times 8000$ nm³, with $M_s = 1400$ kA/m, $J = 30 \times 10^{-12}$ J/m and $\alpha = 0.007$. In addition, $P = 0.32$ and $\xi_{\text{CPP}} = 0.1$ for spin-transfer process. The solid curves are the analytical solution in Eq. (17) and the solid squares in (c) are the simulation data from Fig. 1(b) in Ref. [21] with exactly the same geometric and magnetic parameters.

IV. DW DYNAMICS UNDER PERPENDICULAR POLARIZER

Now $\mathbf{m}_p = \mathbf{m}_y$, thus $\theta_p = \pi/2$ and $\phi_p = \pi/2$. Then $p_\varphi = \cos \varphi$ and Eqs. (11) to (13) are simplified to

$$\frac{1 + \alpha^2}{\gamma} \frac{\eta \dot{q}}{\Delta} = \left[k_H M_s \sin \varphi + \frac{\pi}{2} (\alpha a_J - b_J) \right] \cos \varphi, \quad (22)$$

$$\frac{1 + \alpha^2}{\gamma} \dot{\varphi} = \left[\frac{\pi}{2} (a_J + \alpha b_J) - \alpha k_H M_s \sin \varphi \right] \cos \varphi, \quad (23)$$

$$\frac{\pi^2 \alpha}{6\gamma M_s} \frac{\dot{\Delta}}{\Delta} = \left(\frac{l_0^2}{\Delta^2} - k_E - k_H \sin^2 \varphi \right) + \frac{\pi b_J}{M_s} \sin \varphi. \quad (24)$$

At $t = 0$, $\varphi|_{t=0} = m\pi$ ($m \in \mathbb{Z}$) thus the initial wall velocity is $v|_{t=0} = \eta(-1)^m \Delta_0 \gamma a_J (\alpha - \xi_{\text{CPP}}) \pi / [2(1 + \alpha^2)]$, which is

induced by FLT. For steady traveling-wave mode, we need $\dot{\varphi} = 0$ and $\dot{\Delta} = 0$. This leads to two branches of solution:

$$\begin{aligned} \varphi_0 &= (n + \frac{1}{2})\pi, \quad v_0 = 0, \\ \Delta_2(\varphi_0) &= l_0 \left[k_E + k_H - (-1)^n \frac{\pi b_J}{M_s} \right]^{-1/2}, \end{aligned} \quad (25)$$

and

$$\begin{aligned} \sin \varphi'_0 &= \frac{\pi}{2} \frac{1 + \alpha \xi_{\text{CPP}}}{\alpha} \frac{a_J}{k_H M_s}, \\ v'_0 &= \frac{\pi}{2} \frac{\eta \Delta_2(\varphi'_0) \gamma a_J}{\alpha} \cos \varphi'_0, \\ \Delta_2(\varphi'_0) &= l_0 \left(k_E + k_H \sin^2 \varphi'_0 - \frac{\pi b_J}{M_s} \sin \varphi'_0 \right)^{-1/2}. \end{aligned} \quad (26)$$

Then we perform stability analysis to these two branches. For the one in Eq. (25), after taking similar variation as in Eq. (18) and substituting it into Eq. (23), one has

$$\frac{\partial(\delta\varphi)}{\partial t} = -\frac{\alpha \gamma M_s k_H}{1 + \alpha^2} \left[(-1)^n \frac{\pi}{2} \left(\frac{1}{\alpha} + \xi_{\text{CPP}} \right) \frac{a_J}{k_H M_s} - 1 \right] \cdot \delta\varphi. \quad (27)$$

Now we define

$$J_1 \equiv \frac{4|\xi_{\text{CPP}} - \alpha|}{\pi(1 + \alpha \xi_{\text{CPP}})} J_W > 0. \quad (28)$$

When $J_e > J_1$ (n is even) or $J_e < -J_1$ (n is odd), $(-1)^n (\alpha^{-1} + \xi_{\text{CPP}}) a_J \pi / (2k_H M_s) - 1 > 0$ always holds thus the $\varphi_0 = (n + 1/2)\pi$ solution in the first branch is stable. Next we turn to the wall width of this branch. There exists another critical current density

$$J_\Delta \equiv \frac{1 + \alpha \xi_{\text{CPP}}}{2\alpha \xi_{\text{CPP}}} \frac{k_E + k_H}{k_H} J_1. \quad (29)$$

The existence condition of the wall width, i.e. $k_E + k_H - (-1)^n \pi b_J / M_s > 0$, requires that when n is even (odd), $J_e < J_\Delta$ ($J_e > -J_\Delta$). Generally $J_\Delta \gg J_1$ and out of experimental accessibility, then only J_1 is considered when dealing with stable region. By taking the following variation $\Delta = \Delta_2(\varphi_0) + \delta\Delta$ and putting it into Eq. (24), we have

$$\frac{\pi^2 \alpha}{6\gamma M_s} \frac{\partial(\delta\Delta)}{\partial t} = -\frac{2l_0^2}{\Delta_2^2(\varphi_0)} \cdot \delta\Delta, \quad (30)$$

which means that the zero-velocity solution at $\varphi_0 = (n + 1/2)\pi$ always has a stable wall width.

Then we move to the second branch in Eq. (26). The solution φ'_0 requires $|\sin \varphi'_0| \leq 1$, which is equivalent to $|J_e| \leq J_1$. By setting $\varphi' = \varphi'_0 + \delta\varphi'$ and substituting into Eq. (23), we have

$$\frac{\partial(\delta\varphi')}{\partial t} = -\frac{\alpha \gamma M_s k_H \cos^2 \varphi'_0}{1 + \alpha^2} \cdot \delta\varphi', \quad (31)$$

which means φ'_0 -solution is always stable. The corresponding TDW velocity can be explicitly written out as

$$v'_0 = \frac{\pi}{2} \frac{\eta \Delta_2(\varphi'_0) \gamma a_J}{\alpha} (-1)^m \sqrt{1 - \left(\frac{\pi}{2} \frac{1 + \alpha \xi_{\text{CPP}}}{\alpha k_H M_s} a_J \right)^2}, \quad (32)$$

in which $\varphi'_0|_{t=0} = m\pi$ at $t = 0$. For $|J_e| \ll J_1$, one has

$$v'_0 \approx \frac{\pi}{2} \frac{\eta \Delta_0 \gamma a_J}{\alpha} (-1)^m. \quad (33)$$

It has a mobility larger than that of ‘‘parallel-polarizer’’ case by a factor of $\pi / (2\xi_{\text{CPP}}) \approx 15.7$, which explains the higher efficiency of ‘‘perpendicular-polarizer’’ case. When $|J_e| \rightarrow J_1$, the φ'_0 -solution converges to φ_0 -branch with zero wall velocity.

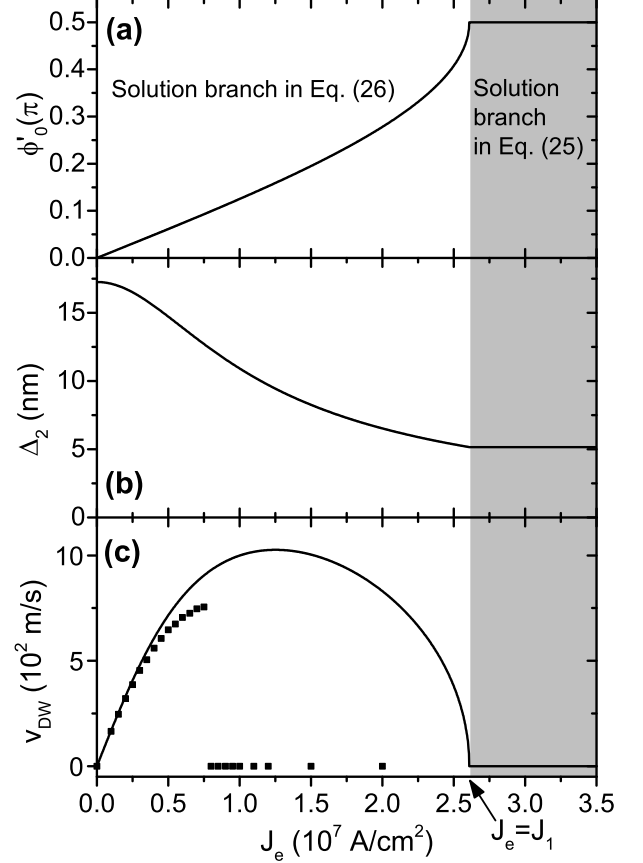


FIG. 3. Dependence of the tilting attitude (a), width (b) and velocity (c) of a DW on current density in a LNSV with CPP configuration and perpendicular polarizer ($\mathbf{m}_p = \mathbf{e}_y$). The geometry and magnetic parameters of the free layer are the same as those in Fig. 2. The solid curves in the white-background area are the solution branch in Eq. (26) and the solid lines in the shaded area are those from Eq. (25). The solid squares in (c) are the simulation data from Fig. 2(b) in Ref. [21] with exactly the same geometric and magnetic parameters.

For the magnetic parameters presented in the end of Sec. II, Eq. (28) provides $J_1 = 0.1183J_W = 2.61 \times 10^7$ A/cm². Then the branch of solution in Eq. (25) [Eq. (26)] is plotted in Fig. 3 by solid line (curve) in shaded (white-background) area for HH DWs ($\eta = +1$), $\varphi_0|_{t=0} = 0$ and $\varphi'_0|_{t=0} = 0$. In addition, simulation data from Fig. 2(b) in Ref. [21] with exactly the same geometric and magnetic parameters are depicted in Fig. 3(c) by solid squares. Clearly when $J_e \leq 0.3 \times 10^7$ A/cm², our analytical wall velocity coincides with the simulated counterpart very well. For larger current density, the wall configura-

tion in simulations will be distorted from the standard Walker profile due to global spin transfers, thus leads to the inconsistency between analytical and simulation results.

V. DW dynamics under planar-transverse polarizer

Now $\mathbf{m}_p = \pm \mathbf{e}_x$, thus $\theta_p = \pi/2$ and $\phi_p = k\pi$ ($k \in \mathbb{Z}$). The dynamical equations take the following form

$$\frac{1 + \alpha^2}{\gamma} \frac{\eta \dot{q}}{\Delta} = \left[k_H M_s \cos \varphi + \frac{\pi}{2} (-1)^k (b_J - \alpha a_J) \right] \sin \varphi, \quad (34)$$

$$\frac{1 + \alpha^2}{\gamma} \dot{\varphi} = - \left[\alpha k_H M_s \cos \varphi + \frac{\pi}{2} (-1)^k (a_J + \alpha b_J) \right] \sin \varphi, \quad (35)$$

$$\frac{\pi^2 \alpha}{6\gamma M_s} \dot{\Delta} = \left(\frac{l_0^2}{\Delta^2} - k_E - k_H \sin^2 \varphi \right) + \frac{\pi b_J}{M_s} (-1)^k \cos \varphi. \quad (36)$$

At $t = 0$, $\varphi|_{t=0} = m\pi$ ($m \in \mathbb{Z}$) thus the initial wall velocity is zero. Next we turn to traveling-wave mode, which requires $\dot{\varphi} = 0$ and $\dot{\Delta} = 0$. This leads to two branches of solution:

$$\varphi_0 = n\pi, \quad v_0 = 0, \quad \Delta_3(\varphi_0) = l_0 \left[k_E - (-1)^{n+k} \frac{\pi b_J}{M_s} \right]^{-1/2}, \quad (37)$$

and

$$\begin{aligned} \cos \varphi'_0 &= -\frac{\pi}{2} (-1)^k \frac{1 + \alpha \xi_{\text{CPP}}}{\alpha} \frac{a_J}{k_H M_s}, \\ v'_0 &= -\frac{\pi}{2} (-1)^k \frac{\eta \Delta_3(\varphi'_0) \gamma a_J}{\alpha} \sin \varphi'_0, \end{aligned} \quad (38)$$

$$\Delta_3(\varphi'_0) = l_0 \left[k_E + k_H \sin^2 \varphi'_0 - \frac{\pi b_J}{M_s} (-1)^k \cos \varphi'_0 \right]^{-1/2}.$$

For the first branch in Eq. (37), the variation in Eq. (18) is still adopted and after similar algebra, Eq. (35) becomes

$$\frac{\partial(\delta\varphi)}{\partial t} = -\frac{\alpha\gamma M_s k_H}{1 + \alpha^2} \left[\frac{\pi}{2} \frac{1 + \alpha \xi_{\text{CPP}}}{\alpha} \frac{(-1)^{n+k} a_J}{k_H M_s} + 1 \right] \cdot \delta\varphi. \quad (39)$$

The stability of φ_0 -solution requires that $(-1)^{n+k}(1 + \alpha \xi_{\text{CPP}}) a_J \pi / (2\alpha k_H M_s) + 1 > 0$, which is equivalent to: $J_e > -J_1$ ($n+k$ is even) or $J_e < J_1$ ($n+k$ is odd). For the wall width of this branch, first its existence condition, i.e. $k_E - (-1)^{n+k} \pi b_J / M_s > 0$, requires that when $n+k$ is even (odd), $J_e < k_E J_\Delta / (k_E + k_H)$ ($J_e > -k_E J_\Delta / (k_E + k_H)$). As pointed in the former subsection, since $J_\Delta \gg J_1$ is usually out of experimental accessibility, only J_1 is considered when dealing with stable region. Then after taking the variation $\Delta = \Delta_3(\varphi_0) + \delta\Delta$ and putting it into Eq. (36), one obtains exactly the same expression as in Eq. (30), leading to a stable wall width of this solution branch.

For the second branch in Eq. (38), it requires $|\cos \varphi'_0| \leq 1$, i.e. $|J_e| \leq J_1$. By writing the variation of tilting angle as $\varphi' =$

$\varphi'_0 + \delta\varphi'$ and substituting into Eq. (35), we have

$$\frac{\partial(\delta\varphi')}{\partial t} = +\frac{\alpha\gamma M_s k_H \sin^2 \varphi'_0}{1 + \alpha^2} \cdot \delta\varphi', \quad (40)$$

which means φ'_0 -solution is always unstable. Any external disturbance on it will driven the wall apart from this solution and converge to the stable branch with zero wall velocity, which means the wall will finally stop after propagating along the LNSV for some distance.

To acquire stable traveling-wave mode motion with finite wall speed for ‘‘planar-transverse polarizer’’ case, the STT coefficients must include $\mathbf{m} \cdot \mathbf{m}_p$ term[11, 42]. The simplest way to do this is replacing the spin polarization P by the spin polarization factor $g \equiv [-4 + (1+P)^3(3 + \mathbf{m} \cdot \mathbf{m}_p)/(4P^{3/2})]^{-1}$ (see Slonczewski’s original description in Ref.[11]) in the definition of the STT coefficient a_J . By introducing two dimensionless parameters b_p and c_p as

$$b_p = \frac{4P^{3/2}}{3(1+P)^3 - 16P^{3/2}}, \quad c_p = \frac{(1+P)^3}{3(1+P)^3 - 16P^{3/2}}, \quad (41)$$

the spin polarization factor can be rewritten as $g = b_p / (1 + c_p P \mathbf{m})$. Following the pioneer work by He in 2013[30], now the 1D magnetic energy functional $\mathcal{E}[\mathbf{m}]$ in Eq. (3) turns to

$$\tilde{\mathcal{E}}[\mathbf{m}] = \mathcal{E}_0[\mathbf{m}] - \mu_0 M_s^2 \xi_{\text{CPP}} \frac{J_e}{J_p} \frac{b_p}{c_p} \ln(1 + c_p P \mathbf{m}), \quad (42)$$

with $J_p \equiv g_e \mu_0 e d M_s^2 / \hbar \approx 2.25 \times 10^9$ A/cm². Correspondingly, the dissipation functional \mathcal{F} in Eq. (6) becomes

$$\frac{\tilde{\mathcal{F}}}{\mu_0 M_s^2} = \frac{\alpha}{2} \frac{\dot{\theta}^2 + \dot{\phi}^2 \sin^2 \theta}{\gamma M_s} - \frac{b_p}{1 + c_p P \mathbf{m}} \frac{J_e}{J_p} (p_\theta \sin \theta \dot{\phi} - p_\phi \dot{\theta}). \quad (43)$$

Putting $\tilde{\mathcal{E}}$ and $\tilde{\mathcal{F}}$ into the generalized Euler-Lagrangian equation (7), we regain the LLG equation in Eq. (8) except for the redefinition of a_J as $\tilde{a}_J = \hbar J_e g / (g_e d e M_s)$.

Still, the generalized Walker profile (see Eq. (10)) is taken as the configuration space of walls. After putting the wall center position $q(t)$, tilting attitude $\varphi(t)$ and width $\Delta(t)$ into Eq. (7) successively, and integrating over the $z \in (-\infty, +\infty)$, a new set of dynamical equations are obtained as

$$\frac{\dot{\varphi} + \alpha \eta \dot{q} / \Delta}{\gamma M_s} = b_p \frac{J_e}{J_p} \left[p_\varphi U(\varphi) - \frac{\xi_{\text{CPP}}}{2c_p} \ln \frac{1 - c_p \cos \theta_p}{1 + c_p \cos \theta_p} \right], \quad (44)$$

$$\begin{aligned} \frac{\alpha \dot{\phi} - \eta \dot{q} / \Delta}{\gamma M_s} &= b_p \frac{J_e}{J_p} \left[\xi_{\text{CPP}} p_\phi U(\varphi) + \frac{1}{2c_p} \ln \frac{1 - c_p \cos \theta_p}{1 + c_p \cos \theta_p} \right] \\ &\quad - k_H \sin \varphi \cos \varphi, \end{aligned} \quad (45)$$

$$\begin{aligned} \frac{\pi^2 \alpha}{6\gamma M_s} \dot{\Delta} &= b_p \frac{J_e}{J_p} \left[\xi_{\text{CPP}} W(\varphi) - p_\varphi U(\varphi) \ln \frac{1 - c_p \cos \theta_p}{1 + c_p \cos \theta_p} \right] \\ &\quad + \left(\frac{l_0^2}{\Delta^2} - k_E - k_H \sin^2 \varphi \right). \end{aligned} \quad (46)$$

with

$$\begin{aligned} U(\varphi) &\equiv \chi / \sqrt{1 - c_p^2 [\sin^2 \theta_p \cos^2(\varphi - \phi_p) + \cos^2 \theta_p]}, \\ W(\varphi) &\equiv \frac{1}{2c_p} \left[\frac{\pi^2}{4} + \frac{1}{4} \ln^2 \frac{1 - c_p \cos \theta_p}{1 + c_p \cos \theta_p} - \chi^2 \right], \\ \chi &\equiv \arccos \frac{c_p \sin \theta_p \cos(\varphi - \phi_p)}{\sqrt{1 - c_p^2 \cos^2 \theta_p}}. \end{aligned} \quad (47)$$

Now we take $\mathbf{m}_p = +\mathbf{e}_x$ as an example of planar-transverse polarizers, thus $\theta_p = \pi/2$ and $\phi_p = 0$. The above equation set then evolves to

$$\frac{1 + \alpha^2}{\gamma M_s} \frac{\eta \dot{q}}{\Delta} = \left[k_H \cos \varphi - (\alpha - \xi_{\text{CPP}}) b_p \frac{J_e}{J_p} \tilde{U}(\varphi) \right] \sin \varphi, \quad (48)$$

$$\frac{1 + \alpha^2}{\gamma M_s} \dot{\varphi} = - \left[(1 + \alpha \xi_{\text{CPP}}) b_p \frac{J_e}{J_p} \tilde{U}(\varphi) + \alpha k_H \cos \varphi \right] \sin \varphi, \quad (49)$$

$$\frac{\pi^2 \alpha}{6\gamma M_s} \frac{\dot{\Delta}}{\Delta} = \left(\frac{l_0^2}{\Delta^2} - k_E - k_H \sin^2 \varphi \right) + \xi_{\text{CPP}} b_p \frac{J_e}{J_p} \tilde{W}(\varphi), \quad (50)$$

in which

$$\begin{aligned} \tilde{U}(\varphi) &= \frac{\tilde{\chi}}{\sqrt{1 - c_p^2 \cos^2 \varphi}}, \quad \tilde{W}(\varphi) = \frac{1}{2c_p} \left(\frac{\pi^2}{4} - \tilde{\chi}^2 \right), \\ \tilde{\chi} &= \arccos(c_p \cos \varphi). \end{aligned} \quad (51)$$

At $t = 0$, $\varphi|_{t=0} = m\pi$ ($m \in \mathbb{Z}$) thus the initial wall velocity is also zero. For steady traveling-wave mode, one has $\dot{\varphi} = 0$ and $\dot{\Delta} = 0$, which leads to two branches of solution:

$$\begin{aligned} \tilde{\varphi}_0 &= n\pi, \quad \tilde{v}_0 = 0, \\ \tilde{\Delta}_3(\tilde{\varphi}_0) &= l_0 \left[k_E - \xi_{\text{CPP}} b_p \frac{J_e}{J_p} \tilde{W}(\tilde{\varphi}_0) \right]^{-1/2}, \end{aligned} \quad (52)$$

and

$$\begin{aligned} \cos \tilde{\varphi}'_0 &= - \frac{1 + \alpha \xi_{\text{CPP}}}{\alpha k_H} b_p \frac{J_e}{J_p} \tilde{U}(\tilde{\varphi}'_0), \\ \tilde{v}'_0 &= \frac{\eta \tilde{\Delta}_3(\tilde{\varphi}'_0) \gamma k_H M_s}{1 + \alpha \xi_{\text{CPP}}} \sin \tilde{\varphi}'_0 \cos \tilde{\varphi}'_0, \end{aligned} \quad (53)$$

$$\tilde{\Delta}_3(\tilde{\varphi}'_0) = l_0 \left(k_E + k_H \sin^2 \tilde{\varphi}'_0 - \xi_{\text{CPP}} b_p \frac{J_e}{J_p} \tilde{W}(\tilde{\varphi}'_0) \right)^{-1/2}.$$

Next we perform stability analysis. For the first branch in Eq. (52), After taking the variation in Eq. (18), Eq. (49) provides

$$\begin{aligned} \frac{\partial(\delta\tilde{\varphi})}{\partial t} &= -\delta\tilde{\varphi} \cdot \frac{\gamma M_s}{1 + \alpha^2} \left\{ (-1)^n (1 + \alpha \xi_{\text{CPP}}) b_p \frac{J_e}{J_p} \times \right. \\ &\quad \left. (1 - c_p^2)^{-1/2} \arccos [(-1)^n c_p] + \alpha k_H \right\}. \end{aligned} \quad (54)$$

The stability of $\tilde{\varphi}_0$ -solution requires that the combination of terms in the curly braces of the above equation must be positive. This leads to $J_e/J_p > j_d$ (n is even) or $J_e/J_p < j_u$ (n is odd), where

$$\begin{aligned} j_u &\equiv \frac{\alpha k_H}{1 + \alpha \xi_{\text{CPP}}} \cdot \frac{\sqrt{1 - c_p^2}}{b_p \arccos(-c_p)}, \\ j_d &\equiv - \frac{\alpha k_H}{1 + \alpha \xi_{\text{CPP}}} \cdot \frac{\sqrt{1 - c_p^2}}{b_p \arccos(c_p)}. \end{aligned} \quad (55)$$

For the wall width of this branch, first its existence condition demands that when n is even (odd), $J_e/J_p < j_{\Delta u}$ ($J_e/J_p > j_{\Delta d}$), in which

$$\begin{aligned} j_{\Delta u} &\equiv \frac{k_E}{\xi_{\text{CPP}}} \cdot \frac{2c_p}{b_p} \cdot \left(\frac{\pi^2}{4} - \arccos^2 c_p \right)^{-1}, \\ j_{\Delta d} &\equiv - \frac{k_E}{\xi_{\text{CPP}}} \cdot \frac{2c_p}{b_p} \cdot \left[\arccos^2(-c_p) - \frac{\pi^2}{4} \right]^{-1}. \end{aligned} \quad (56)$$

Since $\alpha \ll 1$ and $\xi_{\text{CPP}} \ll 1$, $|j_{\Delta u(d)}| \gg |j_{u(d)}|$ and is usually out of experimental accessibility. Thus only $j_{u(d)}$ is considered when dealing with stable region. Then we take the variation $\Delta = \tilde{\Delta}_3(\tilde{\varphi}_0) + \delta\Delta$ and put it into Eq. (50). After standard algebra, we obtains exactly the same expression as that in Eq. (30), implying a stable wall width of this solution branch (see violet solid lines in Fig. 4).

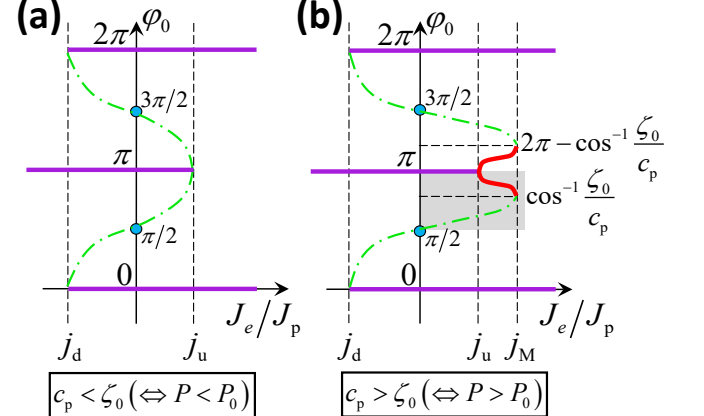


FIG. 4. (Color online) Illustration of the two kind of behaviors of the solution branch in Eq. (53): (a) $c_p < \zeta_0$, (b) $c_p > \zeta_0$. In both cases, the violet solid lines represent the stable solution branch in Eq. (52) with zero velocity, and the green dash-dot curves represent the unstable part of the solution branch in Eq. (53). In addition, the red solid curves in (b) indicate the stable part of the solution branch in Eq. (53). The shaded area in (b) corresponds to the detailed calculations in Fig. 5.

Next we turn to the branch in Eq. (53). By rewriting the first equation as $J_e/J_p = -\alpha k_H \cos \tilde{\varphi}'_0 (1 - c_p^2 \cos^2 \tilde{\varphi}'_0)^{1/2} / [(1 + \alpha \xi_{\text{CPP}}) b_p \arccos(c_p \cos \tilde{\varphi}'_0)]$ and analyzing its monotonicity, the permitted current density range of this branch can be obtained. Obviously $J_e(\tilde{\varphi}'_0) = J_e(2\pi - \tilde{\varphi}'_0)$, thus the discussion

for $\tilde{\varphi}'_0 \in [0, \pi]$ is enough which ensures $\sin \tilde{\varphi}'_0 \geq 0$. After standard calculus, one has

$$\frac{d}{d\tilde{\varphi}'_0} \left(\frac{J_e}{J_p} \right) = \frac{\alpha k_H \sin \tilde{\varphi}'_0}{(1 + \alpha \xi_{\text{CPP}}) b_p} \cdot \frac{f(\zeta)}{\sqrt{1 - \zeta^2} \cdot \arccos \zeta}, \quad (57)$$

with

$$f(\zeta) = (1 - 2\zeta^2) \arccos \zeta + \zeta \sqrt{1 - \zeta^2}, \quad \zeta \equiv c_p \cos \tilde{\varphi}'_0. \quad (58)$$

On the other hand, by writing the variation of tilting angle as $\tilde{\varphi}' = \tilde{\varphi}'_0 + \delta\tilde{\varphi}'$ and substituting into Eq. (49), we have

$$\frac{\partial(\delta\tilde{\varphi}')}{\partial t} = \frac{\alpha \gamma M_s k_H \sin^2 \tilde{\varphi}'_0}{(1 + \alpha^2)(1 - \zeta^2) \arccos \zeta} f(\zeta) \cdot \delta\tilde{\varphi}', \quad (59)$$

The monotonicity analysis on $f(\zeta)$ provides us a critical value $\zeta_0 = -0.6256$ ($\Leftrightarrow P_0 = 0.3704$), which is the zero point of $f(\zeta)$ and separates two kinds of behaviors of the second solution branch. When $c_p < \zeta_0$ ($\Leftrightarrow P < P_0$), we always have $f(\zeta) > 0$. This fact has two consequences: from Eq. (57), J_e/J_p is an increasing function on $\tilde{\varphi}'_0 \in [0, \pi]$ thus acquires its minimum (indeed j_d) at $\tilde{\varphi}'_0 = 0$ and maximum (j_u) at $\tilde{\varphi}'_0 = \pi$ (see Fig. 4(a)). However, Eq. (59) tells us that now this whole branch remains unstable thus is not physically preferred. When $c_p > \zeta_0$ ($\Leftrightarrow P > P_0$), $f(\zeta)$ first increases when $\tilde{\varphi}'_0$ runs from 0 to $\arccos(\zeta_0/c_p)$ and then decreases when $\tilde{\varphi}'_0$ exceeds $\arccos(\zeta_0/c_p)$ to π . Correspondingly, J_e/J_p increases from j_d to $j_M = 0.2172\alpha k_H / [(1 + \alpha \xi_{\text{CPP}}) b_p c_p]$ and then decreases to j_u , as illustrated in Fig. 4(b). Meantime, from Eq. (59) only when $\arccos(\zeta_0/c_p) < \tilde{\varphi}'_0 < 2\pi - \arccos(\zeta_0/c_p)$ the solution branch in Eq. (53) is stable, which has been marked by red curves in Fig. 4(b).

Now we summarize what happens physically when the CPP current density J_e increases from 0 to large positive value. If the wall initially lies in the easy xz -plane with $\varphi|_{t=0} = 0$, i.e. the magnetization at wall center is parallel with the polarizer, then it always stays in this state with zero velocity as J_e increases. While if the wall initially lies with $\varphi|_{t=0} = \pi$, i.e. the magnetization at wall center is anti-parallel with the polarizer, it keeps on staying in this state until J_e/J_p increases to j_u . When J_e is further enhanced a little bit, something interesting happens. For the case where the polarizer is not strong enough ($P < P_0$), the wall will “jump” to $\varphi = 0$ state (through $\pi \rightarrow 0$ or $\pi \rightarrow 2\pi$ route depending on the nature of external disturbances) and keep it going. On the other hand, if the polarizer is strong enough ($P_0 < P \leq 1$), the wall will evolve smoothly into one of the two stable part of the solution branch in Eq. (53). Likely, which one it runs into is determined by the nature of external disturbances. As J_e/J_p increases from j_u to j_M , the wall acquires a finite velocity as shown by the second equation of Eq. (53). When J_e/J_p exceeds j_M , the wall will jump to its nearest zero-velocity branch under external disturbances and then keep in this state.

Next we do some numerical estimation works. As indicated, to obtain stable propagating walls the spin polarization P should satisfy $P > P_0 = 0.3704$. Here we take $P = 0.6$ as

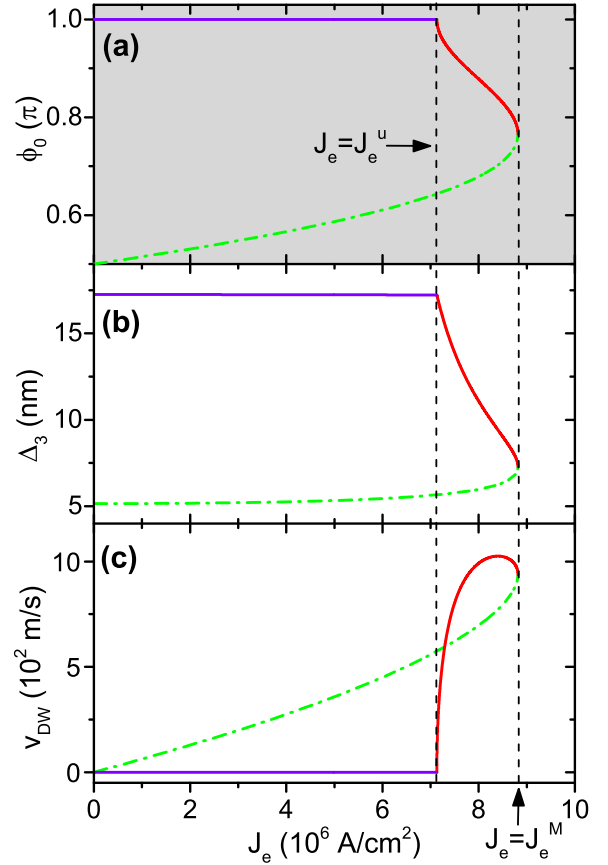


FIG. 5. (Color online) Dependence of the tilting attitude (a), width (b) and velocity (c) of a DW on current density in a LNSV with CPP configuration and planar-transverse polarizer ($\mathbf{m}_p = +\mathbf{e}_x$). The sub-figure (a) corresponds to the shaded area in Fig. 4(b). The geometry and magnetic parameters of the free layer are the same as those in Fig. 2, except that the spin polarization is changed to $P = 0.6$. The violet solid lines are those from the stable zero-velocity branch in Eq. (52). The red solid (green dash-dot) curves comes from the stable (unstable) part of the finite-velocity branch in Eq. (53).

an example and keep all other parameters the same as those in the end of Sec. II. Then $b_p = 0.3832$ and $b_p = 0.8442$, thus the extremal point is $\varphi_0^M = \arccos(\zeta_0/c_p) = 0.7657\pi$. The upper limit of the current density for the stable zero-velocity branch in Eq. (52) is $J_e^u = j_u \cdot J_p = 7.13 \times 10^6$ A/cm². Meantime, the upper limit of the current density for the stable finite-velocity branch in Eq. (53) is $J_e^M = j_M \cdot J_p = 8.82 \times 10^6$ A/cm². These two values are both not high for real applications. Then the tilting attitude, width and velocity of the TT ($\eta = -1$) DW corresponding to the shaded area in Fig. 4(b) are calculated and plotted in Fig. 5. We focus on the red curves which are the stable part of the finite-velocity branch in Eq. (53). It is interesting to find that around 8.40×10^6 A/cm² the wall can even propagate along the LNSV at a velocity as high as 1025 m/s. After comparing with Fig. 3(c), one can find that the planar-transverse polarizer has the same current efficiency as the perpendicular polarizer. To our knowledge,

this has never been reported before in existing studies. Another attracting quantity is the “differential mobility” (dv/dJ_e) around $J_e = J_e^u$ ($\phi'_0 = \pi$). From Eqs. (53) and (57), one has $dv'_0/dJ_e = (dv'_0/d\phi'_0)(dJ_e/d\phi'_0)^{-1} \propto 1/\sin\phi'_0 \rightarrow \infty$. This means that a slight increase of J_e above J_e^u will lead to considerable increase of wall velocity. This behavior should have great application potential in designing high-speed nanodevices based on DW propagation in LNSVs.

At last, for $\mathbf{m}_p = -\mathbf{e}_x$, similar discussions can be performed. It turns out that stable parts of the solution branch with finite wall velocity can only appear for negative J_e region ($-j_M \leq J_e/J_p < -j_u$). However this is not physical since the electrons must be polarized first (passing through the pinned layer) so as to drive the wall in the free layer.

VI. DW BOOSTING BY UTMFS

To further boost TDW propagation, a UTMF

$$\mathbf{H}_{\text{TMF}} = H_{\perp}(\cos\Phi_{\perp}, \sin\Phi_{\perp}, 0) \quad (60)$$

is exerted onto this LNSV, with H_{\perp} and Φ_{\perp} being the UTMF strength and orientation, respectively. However, rigorous profile and velocity of TDWs under an arbitrary UTMF are hard to obtain due to the mismatch between symmetries in different energy terms in transverse direction. Since we focus on the traveling-mode at low current density, the 1D-AEM[32–36] shall provide useful information. In this approach, the dynamical behavior of a TDW is viewed as the response of its static profile to external stimuli (here is the injected current), which leads to simultaneous rescaling of current density and wall velocity (or inverse of time). Therefore, it is the manifestation of linear response theory in nanomagnetism. Meanwhile, the pinned layer is assumed to be unaffected by UTMFs, which is a harmless simplification and will not affect our main results since we focus on magnetization dynamics in the free layer. Recalling the results in the previous three sections, clearly for DWs moving under planar-transverse polarizers, the 1D-AEM is not applicable since stable DW motion with finite velocity can only be excited when the current density exceeds a finite lower limit. Hence in this section, we present the results for parallel and perpendicular polarizers. For simplicity, the STT coefficients are still assumed to be $\mathbf{m} \cdot \mathbf{m}_p$ -independent.

VI.A Parallel polarizer

The 1D-AEM needs static profiles of TDWs as the basis to calculate the response of the system under external stimuli. Depending on the UTMF strength, static TDWs take different profiles. Therefore we will discuss the “small UTMF” and “finite UTMF” cases separately.

For small UTMFs, the CCP current density, UTMF, and inverse of time are rescaled simultaneously,

$$a_J = \varepsilon a_J^0 (b_J = \varepsilon b_J^0), H_{\perp} = \varepsilon h_{\perp}, 1/t = \varepsilon(1/\tau), \quad (61)$$

where ε is a dimensionless infinitesimal. The real solution of the LLG equation is expanded as follows,

$$\Omega(z, t) = \Omega_0(z, \tau) + \varepsilon \Omega_1(z, \tau) + O(\varepsilon^2), \quad \Omega = \theta, \phi. \quad (62)$$

Putting them back into the original LLG equation (8), the solutions to the zeroth-order equation are just Eq. (9). At the first order of ε , with the help of zeroth-order solutions, the differential equation about θ_1 reads,

$$F_s = \mathcal{L}\theta_1, \quad \mathcal{L} \equiv \frac{2J}{\mu_0 M_s} \left(-\frac{d^2}{dz^2} + \frac{\theta_0'''}{\theta_0'} \right), \quad (63)$$

$$F_s \equiv \left[\frac{\eta \alpha(z_0) \tau}{\gamma \Delta_0} - b_J^0 \right] \sin\theta_0 + (-1)^n h_{\perp} \cos\theta_0 \cos\Phi_{\perp},$$

where $(z_0)_{\tau} \equiv dz_0/d\tau$ and a prime means d/dz . The superscript “s” in variables indicates the “small UTMF” case and holds in the rest of this paper. Note that \mathcal{L} is the same 1D self-adjoint Schrödinger operator as given in Refs. [32–36]. Following the “Fredholm alternative”, by demanding θ_0' (kernel of \mathcal{L}) to be orthogonal to the function F^s defined in Eq. (63), and noting that $\langle \theta_0', \sin\theta_0 \rangle = 2\eta$ and $\langle \theta_0', \cos\theta_0 \rangle = 0$, we obtain the TDW velocity in traveling-wave mode under small UTMFs,

$$V_s = \varepsilon(z_0)_{\tau} = \eta \gamma \Delta_0 b_J / \alpha, \quad (64)$$

which reproduces the rigorous result in Eq. (17).

For finite UTMFs, we rescale the current density and the TDW velocity V^f simultaneously, thus

$$a_J = \varepsilon a_J^0 (b_J = \varepsilon b_J^0), \quad V^f = \varepsilon v. \quad (65)$$

in which the superscript “f” denotes the “finite UTMF” case. By defining the traveling coordinate

$$\tilde{z} \equiv z - V_{\text{CPPz}}^f t = z - \varepsilon v t, \quad (66)$$

$\theta(z, t)$, $\phi(z, t)$ are expanded as follows,

$$\Omega(z, t) = \Omega_0(\tilde{z}) + \varepsilon \Omega_1(\tilde{z}) + O(\varepsilon^2), \quad \Omega = \theta, \phi. \quad (67)$$

Substituting Eq. (67) into Eq. (8), an approximate polar angle profile θ_0 (solution to the zeroth-order equations) of the wall is obtained as,

$$\ln \frac{\sin\theta_0 - \sin\theta_{\infty}}{1 + \cos(\theta_0 + \theta_{\infty})} = \frac{\eta \tilde{z}}{\Delta(\phi_{\infty}) / \cos\theta_{\infty}}, \quad (68)$$

with

$$\phi_{\infty} = \tan^{-1} [k_E \tan\Phi_{\perp} / (k_E + k_H)],$$

$$\theta_{\infty} = \sin^{-1} \frac{H_{\perp}}{M_s \sqrt{k_E^2 \cos^2\phi_{\infty} + (k_E + k_H)^2 \sin^2\phi_{\infty}}}, \quad (69)$$

$$\Delta(\phi_{\infty}) = l_0 (k_E + k_H \sin^2\phi_{\infty})^{-1/2},$$

in which θ_{∞} (ϕ_{∞}) is the polar (azimuthal) angle of magnetization in the domains. At the first order of ε , after similar

process as in axial-field-driven case[34], the differential equation about θ_1 is

$$\mathcal{L}(\gamma\theta_1) = F_f \equiv v\gamma^{-1}(\alpha\theta'_0 - \sin\theta_0\phi'_0) - b_J^0 \sin\theta_0. \quad (70)$$

where a ‘‘prime’’ means d/dz . Again, θ'_0 (kernel of \mathcal{L}) should be orthogonal to the function F_f . Noting that $\langle\theta'_0, \theta'_0\rangle = [2\cos\theta_\infty - (\pi - 2\theta_\infty)\sin\theta_\infty]/\Delta(\phi_\infty)$, $\langle\theta'_0, \sin\theta_0\phi'_0\rangle = 0$, and $\langle\theta'_0, \sin\theta_0\rangle = 2\eta\cos\theta_\infty$, TDW velocity in traveling-wave mode under finite UTMF is,

$$V_f = u(\theta_\infty) \frac{\eta\gamma\Delta(\phi_\infty)b_J}{\alpha}, \quad (71)$$

$$u(\theta_\infty) = \frac{2\cos\theta_\infty}{2\cos\theta_\infty - (\pi - 2\theta_\infty)\sin\theta_\infty}.$$

This clearly shows that UTMFs can boost TDW propagation by manipulating its width by the factor $u(\theta_\infty)$ (see Ref. [34]).

VI.B Perpendicular polarizer

For small UTMFs, the CPP current, UTMF, and inverse of time are rescaled together as in Eq. (61). Then the same expansion and substitution operation as in parallel-polarizer case are performed. The zeroth-order solution still takes the form of Eq. (9). Furthermore, the differential equation about θ_1 is,

$$\mathcal{L}\theta_1 = \frac{\eta\alpha(z_0)\tau \sin\theta_0}{\gamma\Delta_0} + (-1)^n (h_\perp \cos\theta_0 \cos\Phi_\perp - a_J^0). \quad (72)$$

Thus the TDW velocity under small UTMFs is,

$$V_s = \varepsilon(z_0)\tau = (-1)^n \eta\pi\gamma\Delta_0 a_J / (2\alpha), \quad (73)$$

which is also the $\phi'_0 \rightarrow n\pi$ limit of Eq. (26).

For finite UTMFs, after similar procedure as in ‘‘parallel polarizer’’ case, the differential equation about θ_1 is,

$$\mathcal{L}\theta_1 = \frac{v}{\gamma}(\alpha\theta'_0 - \sin\theta_0\phi'_0) - a_J^0 \cos\phi_0 + b_J^0 \cos\theta_0 \sin\phi_0. \quad (74)$$

Noting that $\langle\theta'_0, \cos\phi_0\rangle \approx \eta(\pi - 2\theta_\infty)\cos\phi_\infty$ and $\langle\theta'_0, \cos\theta_0 \sin\phi_0\rangle = 0$, one has,

$$V_f \approx \omega(\theta_\infty) \frac{\eta\gamma\Delta(\phi_\infty)a_J}{\alpha} \cos\phi_\infty, \quad (75)$$

$$\omega(\theta_\infty) = \frac{\pi - 2\theta_\infty}{2\cos\theta_\infty - (\pi - 2\theta_\infty)\sin\theta_\infty}.$$

Simple calculus shows that $\omega(\theta_\infty)$ has similar divergent behavior as $u(\theta_\infty)$ when $H_\perp \rightarrow H_\perp^{\max}$, which leads to considerable boosting of TDW motion. More interestingly, in LNSVs with perpendicular polarizers, TDW motion can be manipulated not only by UTMF strength (via ‘‘ $\omega(\theta_\infty)$ ’’) but also its orientation (via ‘‘ $\cos\phi_\infty$ ’’). This is due to the fact that now the polarized electrons always act as an extra time-dependent effective field in hard axis (since $\mathbf{m}_p = \mathbf{e}_y$). For TDWs with $\phi_\infty \neq n\pi$, the magnetization in the wall rotates around the effective field hence results in a translational displacement of TDW along ‘‘ $\eta\mathbf{e}_z$ ’’ direction. On the other hand, the projection of Slonczewski torque to the hard axis \mathbf{e}_y contributes to ‘‘ $\cos\phi_\infty$ ’’. These lead to the final ‘‘ $\eta\cos\phi_\infty$ ’’ factor in Eq. (75).

VII. SUMMARY

In this work, DW dynamics in LNSVs with CPP configurations are systematically investigated within Lagrangian framework. For $\mathbf{m} \cdot \mathbf{m}_p$ -independent STT coefficients, analytical results for parallel and perpendicular polarizers perfectly explain the existing simulation findings. For planar-transverse polarizers, all stable solutions are those with zero wall velocity. Then we introduce Slonczewski’s original description on STT coefficients which are $\mathbf{m} \cdot \mathbf{m}_p$ -dependent. It turns out that stable traveling-wave motion of TDWs with finite velocity can survive for strong enough spin polarization of charge current. Interestingly, planar-transverse polarizers have nearly the same current efficiency as perpendicular ones. More importantly, now the wall has infinite ‘‘differential mobility’’ around the onset of stable wall excitation. At last, further boosting of TDWs by external UTMFs are investigated with help of 1D-AEM and turns out to be efficient.

ACKNOWLEDGEMENT

This work is supported by the National Natural Science Foundation of China (Grants No. 11374088). Z. An also acknowledges the support from the Hebei Province Department of Education (GCC2014025).

* jlu@hebtu.edu.cn

- [1] F. H. D. Leeuw, R. V. D. Doel, and U. Enz, Rep. Prog. Phys. **43**, 689 (1980).
- [2] Y. Tserkovnyak, A. Brataas, G. E. W. Bauer, and B. I. Halperin, Rev. Mod. Phys. **77**, 1375 (2005).
- [3] M. Kläui, J. Phys.: Condens. Matter **20**, 313001 (2008).
- [4] D. A. Allwood, G. Xiong, C. C. Faulkner, D. Atkinson, D. Petit, and R. P. Cowburn, Science, **309**, 1688 (2005).
- [5] M. Hayashi, L. Thomas, R. Moriya, C. Rettner, and S. S. P. Parkin, Science **320**, 209 (2008).
- [6] J. H. Franken, H. J. M. Swagten, and B. Koopmans, Nat. Nanotechnol. **7**, 499 (2012).
- [7] J. Münchenberger, G. Reiss, and A. Thomas, J. Appl. Phys. **111**, 07D303 (2012).
- [8] S. S. P. Parkin and S.-H. Yang, Nat. Nanotechnol. **10**, 195 (2015).
- [9] N. L. Schryer and L. R. Walker, J. Appl. Phys. **45**, 5406 (1974).
- [10] L. Berger, Phys. Rev. B **54**, 9353 (1996).
- [11] J. Slonczewski, J. Magn. Magn. Mater. **159**, L1 (1996).
- [12] Z. Li and S. Zhang, Phys. Rev. Lett. **92**, 207203 (2004).
- [13] G. Tatara, H. Kohno, and J. Shibata, Phys. Rep. **468**, 213 (2008).
- [14] F. Schlickeiser, U. Ritzmann, D. Hinzke, and U. Nowak, Phys. Rev. Lett. **113**, 097201 (2014).
- [15] X. S. Wang and X. R. Wang, Phys. Rev. B **90**, 014414 (2014).
- [16] J. Grollier, D. Lacour, V. Cros, A. Hamzic, A. Vaurès, and A. Fert, D. Adam and G. Faini, J. Appl. Phys. **92**, 4825 (2002).
- [17] J. Grollier, P. Boulenc, V. Cros, A. Hamzic, A. Vaurès, A. Fert, and G. Faini, Appl. Phys. Lett. **83**, 509 (2003).

- [18] C. K. Lim, T. Devolder, C. Chappert, J. Grollier, V. Cros, A. Vaurès, A. Fert, and G. Faini, *Appl. Phys. Lett.* **84**, 2820 (2004).
- [19] A. Rebei and O. Mryasov, *Phys. Rev. B* **74**, 014412 (2006).
- [20] K. Kawabata, M. Tanizawa, K. Ishikawa, Y. Inoue, M. Inuishi, and T. Nishimura, presented at the 2011 International Conference on Simulation of Semiconductor Processes and Devices, 2011 (unpublished).
- [21] A. V. Khvalkovskiy, K. A. Zvezdin, Ya. V. Gorbunov, V. Cros, J. Grollier, A. Fert, and A. K. Zvezdin, *Phys. Rev. Lett.* **102**, 067206 (2009).
- [22] C. T. Boone, J. A. Katine, M. Carey, J. R. Childress, X. Cheng, and I. N. Krivorotov, *Phys. Rev. Lett.* **104**, 097203 (2010).
- [23] A. Chanthbouala, R. Matsumoto, J. Grollier, V. Cros, A. Anane, A. Fert, A. V. Khvalkovskiy, K. A. Zvezdin, K. Nishimura, Y. Nagamine, H. Maehara, K. Tsunekawa, A. Fukushima, and S. Yuasa, *Nat. Phys.* **7**, 626 (2011).
- [24] P. J. Metaxas, J. Sampaio, A. Chanthbouala, R. Matsumoto, A. Anane, A. Fert, K. A. Zvezdin, K. Yakushiji, H. Kubota, A. Fukushima, S. Yuasa, K. Nishimura, Y. Nagamine, H. Maehara, K. Tsunekawa, V. Cros, and J. Grollier, *Sci. Rep.* **3**, 1829 (2013).
- [25] J. Sampaio, S. Lequeux, P. J. Metaxas, A. Chanthbouala, R. Matsumoto, K. Yakushiji, H. Kubota, A. Fukushima, S. Yuasa, K. Nishimura, Y. Nagamine, H. Maehara, K. Tsunekawa, V. Cros, and J. Grollier, *Appl. Phys. Lett.* **103**, 242415 (2013).
- [26] S. Pizzini, V. Uhlř, J. Vogel, N. Rougemaille, S. Laribi, V. Cros, E. Jiménez, J. Camarero, C. Tieg, and E. Bonet, *Appl. Phys. Express* **2**, 023003 (2009).
- [27] V. Uhlř, S. Pizzini, N. Rougemaille, J. Novotný, V. Cros, E. Jiménez, G. Faini, L. Heyne, F. Sirotti, C. Tieg, A. Bendouan, F. Maccherozzi, R. Belkhou, J. Grollier, A. Anane, and J. Vogel, *Phys. Rev. B* **81**, 224418 (2010).
- [28] V. Uhlř, S. Pizzini, N. Rougemaille, V. Cros, E. Jiménez, L. Ranno, O. Fruchart, M. Urbánek, G. Gaudin, J. Camarero, C. Tieg, F. Sirotti, E. Wagner, and J. Vogel, *Phys. Rev. B* **83**, 020406(R) (2011).
- [29] V. Uhlř, J. Vogel, N. Rougemaille, O. Fruchart, Z. Ishaque, V. Cros, J. Camarero, J. C. Cezar, F. Sirotti, and S. Pizzini, *J. Phys.: Condens. Matter* **24**, 024213 (2012).
- [30] P.-B. He, *Eur. Phys. J. B* **86**, 412 (2013).
- [31] J. Shibata, G. Tatara, and H. Kohno, *Journal of Physics D: Applied Physics* **44**, 384004 (2011).
- [32] A. Goussev, R. G. Lund, J. M. Robbins, V. Slastikov, and C. Sonnenberg, *Phys. Rev. B* **88**, 024425 (2013).
- [33] A. Goussev, R. G. Lund, J. M. Robbins, V. Slastikov, and C. Sonnenberg, *Proc. R. Soc. A* **469**, 20130308 (2013).
- [34] J. Lu, *Phys. Rev. B* **93**, 224406 (2016).
- [35] M. Li, J. B. Wang, and J. Lu, *Sci. Rep.* **7**, 43065 (2017).
- [36] M. Yu, M. Li, and J. Lu, *Nanomaterials* **9**, 128 (2019).
- [37] K.-J. Lee, M. D. Stiles, H.-W. Lee, J.-H. Moon, K.-W. Kim, and S.-W. Lee, *Phys. Rep.* **531**, 89 (2013).
- [38] M. Chshiev, A. Manchon, A. Kalitsov, N. Ryzhanova, A. Vedyayev, N. Strelkov, W. H. Butler, and B. Dieny, *Phys. Rev. B* **92**, 104422 (2015).
- [39] R. D. McMichael and M. J. Donahue, *IEEE Trans. Magn.* **33**, 4167 (1997).
- [40] Y. Nakatani, A. Thiaville, and J. Miltat, *J. Magn. Magn. Mater.* **290**, 750 (2005).
- [41] N. Rougemaille, V. Uhlř, O. Fruchart, S. Pizzini, J. Vogel, and J. C. Toussaint, *Appl. Phys. Lett.* **100**, 172404 (2012).
- [42] P. Chureemart, I. D'Amico, and R. W. Chantrell, *J. Phys.: Condens. Matter* **27**, 146004 (2015).